RESEARCH ARTICLE

SIW Based D-Band Single and 2 × 2 MIMO Elliptically Tapered Slot Antenna

AMIR ALTAF[ID], (Member, IEEE), AND MUNKYO SEO[ID], (Senior Member, IEEE)

Department of Electrical and Computer Engineering, Sungkyunkwan University, Suwon 440-746, South Korea

Corresponding author: Munkyo Seo (mkseo@skku.edu)

ABSTRACT In this paper, the substrate integrated waveguide (SIW) based single and 2 × 2 multiple input multiple output (MIMO) elliptically tapered slot antennas (ETSA) have been demonstrated at the D-band. The width of the coupling SIW line is selected to operate at the TE_{10}-mode within the frequency range of interest. The elliptically tapered opening is designed in front of the upper and lower metal layers at the radiating end of the SIW line. The outer sides of elliptically tapered metal extensions are corrugated to improve the impedance matching. For measurement, three separate SIW based transitions working at different frequency ranges are integrated with single SIW ETSA and named as Ant-1, Ant-II, and Ant-III. A setup was constructed for far-field measurements within the laboratory where only the 2D radiation patterns and gains can be measured. The Ant-I, Ant-II, and Ant-III prototypes achieved a measured $|S_{11}| < -10$ dB of 20 GHz (110–130 GHz), 28.6 GHz (130–158.6 GHz) and 16 GHz (154–170 GHz) with peak gains of 12.85, 12.86, and 10.4 dBi, respectively. For 2 × 2 MIMO versions, the S-parameters, and condition number for line-of-sight scenario were measured.

INDEX TERMS D-band, multiple input multiple output (MIMO), substrate integrated waveguide (SIW) technology, tapered slot antenna, terahertz antenna.

I. INTRODUCTION

In recent years, there has been a lot of interest in studies on the sixth generation (6G) of modern communication, which aims to deliver data rates up to 1 Tpbs with low latency and wide bandwidth using tera-hertz frequencies. One likely contender for developing 6G transceivers is D-band (110-170 GHz). Several technologies have been used in the design of 6G antennas [1]. By avoiding off-chip integration losses, on-chip antennas result in a compact design and good transceiver performance at the expense of reduced radiation efficiency and higher cost [2]. Although [3] proposes localized back etching (LBE) for gain enhancement, the design and manufacturing complexity will be significantly increased due to the use of micro-machining. Antennas-in-package (AiP) have been demonstrated, however the measured −10 dB impedance bandwidth (IBW) is narrower [4], [5]. A low-temperature

co-fired ceramics (LTCC) process is another reasonable alternative for the design of D-band antennas. A microstrip slot antenna with substrate integrated waveguide (SIW) fence generates a −10 dB IBW of 22 GHz (114–136 GHz) with a gain of 6 dBi at 122.5 GHz [6]. A 2 × 2 LTCC horn antenna is designed with a measured −10 dB IBW of 9 GHz and a simulated gain of 13.3 dBi [7]. Similarly, an 8 × 8 array of the SIW cavity embedded patch was designed in the LTCC process with −10 dB IBW of 9.8 GHz (136.7–146.5 GHz) [8]. Metallic antennas have also been designed at the D-band for high gain applications. A 16 × 16 array antenna was designed in the gap waveguide technology, offering a simulated −10 dB IBW of 14 GHz (134–148 GHz) with a simulated gain of more than 19 dBi [9]. Similarly 32 × 32 and 64 × 64-element arrays were designed utilizing the diffusion bonding of laminated thin metal plates, achieving −10 dB IBWs of 15 GHz (119-134 GHz) and 14.5 GHz (118.5–133 GHz) with gains higher than 38 dBi and 43 dBi, respectively [10]. The D-band antennas were also created

The associate editor coordinating the review of this manuscript and approving it for publication was Hussein Attia[ID].

using 3D printing technology. One of the designs in [11] employs the selective laser melting (SLM) technique to construct a horn antenna that was excited via a slot engraved in the SIW cavity. The measurements revealed −10 dB IBW of 18.9 GHz (129.5–156.5 GHz) with a peak gain of 15.46 dBi. Similarly, a resonant cavity antenna (RCA) was fabricated using the methods of direct metal laser sintering (DLMS), and dielectric printing with a metal coating. The measurements demonstrated −10 dB IBWs of 40 GHz (130–170 GHz) for both antennas with a gain > 7 dBi for DLMS and > 5 dBi for metal-coated dielectric printed antenna [12]. Due to its advantages of low manufacturing cost and simple integration with transceiver chips, printed circuit board (PCB) technology has also been used to create D-band antennas. According to [13], a differential fed 1 × 8 microstrip patch antenna array produces a narrow −10 dB IBW of 7 GHz with a peak gain of 12.98 dBi. Similarly, the earlier referenced work [11] also demonstrated a SIW integrated microstrip antenna yielding −10 dB IBW of 29.1 GHz (125.3–154.4 GHz) with a peak gain of 7.26 dBi. The authors in [14] presented an L-probe fed differential dual-polarized patch antenna with a soft surface where a 23.4 GHz of the measured −9.4 dB IBW lies in the D-band frequency range and a peak gain of 9.5/9.8 dBi is achieved for port1/port2. A recent study proposed a wide-band stacked patch antenna on a flexible material where 27.5 GHz (110-137.5 GHz) of −10 dB IBW overlaps with the D-band frequency range and the design achieved a peak gain of 7.95 dBi [15]. Similarly, we presented a wide-band SIW-cavity based slot antenna with a wide −10 dB IBW of 60 GHz that encompasses the whole D-band with a peak gain of 10.8 dBi [16].

In this paper, we present a wide-band end-fire SIW-based elliptically tapered slot antenna (ETSA). The width of the SIW line is chosen such that TE_{10}-mode is excited across the entire D-band. The dimensions of the tapered opening were optimized to yield low magnitude of the reflection coefficients and higher gain within the band of operation. The corrugations used in the design also minimize the magnitude of the reflection coefficients and stabilize the gain. Three waveguide (WG)-SIW transitions operating over different frequency ranges are designed and integrated with the proposed antenna for measurement purposes. The integrated antenna prototypes, known as Ant-I, Ant-II, and Ant-III, have been manufactured and produced −10 dB IBWs of 20 GHz (110–130 GHz), 28.6 GHz (130–158.6 GHz) and 16 GHz (154–170 GHz) along with the measured peak gains of 12.85 dBi, 12.86 dBi, and 10.4 dBi, respectively. Since, the MIMO antennas have not been thoroughly investigated for the D-band applications, the D-band 2 × 2 MIMO antennas were designed, fabricated, and measured using the proposed integrated antennas (Ant-I, Ant-II, and Ant-III). The isolation for all three 2 × 2 MIMO antennas exceeds 36.9 dB. The complex coefficients of the channel matrix were then measured for all three integrated MIMO antennas in the Line-of-Sight (LOS) scenario using the N5244B PNA-X network analyzer with D-band extenders. Based on the measured
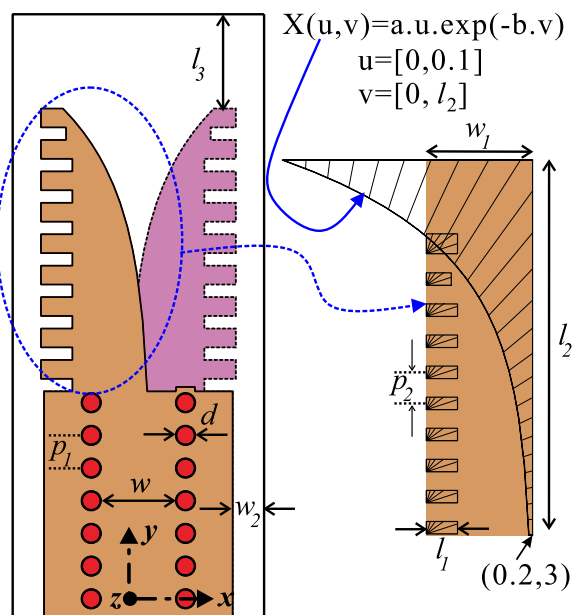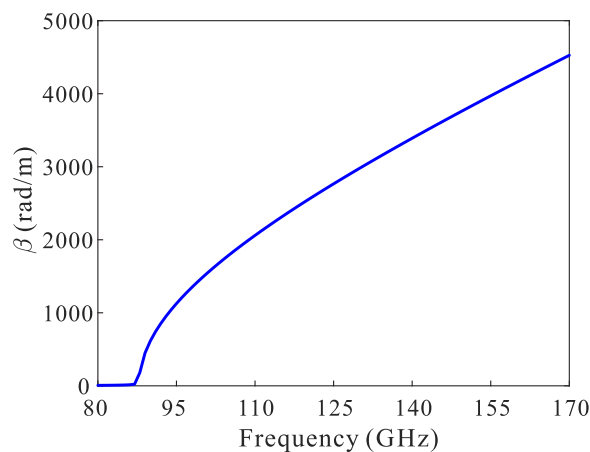

FIGURE 1. Geometry of the proposed design.

FIGURE 2. Simulated propagation constant β of the SIW line with width *w*.

channel matrix, the condition numbers versus frequency is also plotted.

The content of the article is as follows. Section II discusses the SIW ETSA antenna design, parametric study, fabrication, measurement, and comparison with previous studies. Section III examines the design, fabrication, and measurement of the 2 × 2 MIMO antenna, where in measurements the S-parameters and condition number are plotted. Section IV draws the article to a conclusion.

II. SINGLE ANTENNA DESIGN AND MEASUREMENTS
A. DESIGN DESCRIPTION
Fig. 1 depicts the geometry of the SIW based ETSA. The antenna is designed on a 10 mil thick Rogers RT/Duroid 5880 substrate. To connect the top and bottom metal layers, an array of vias with diameter *d* and period p_1 is used to
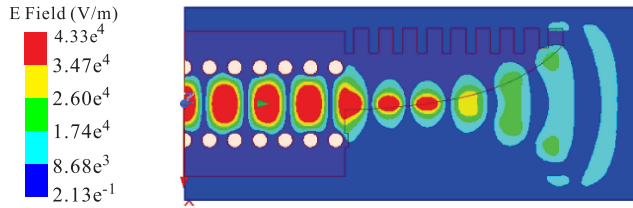
FIGURE 3. Simulated E-field distribution of the proposed antenna at 140 GHz.
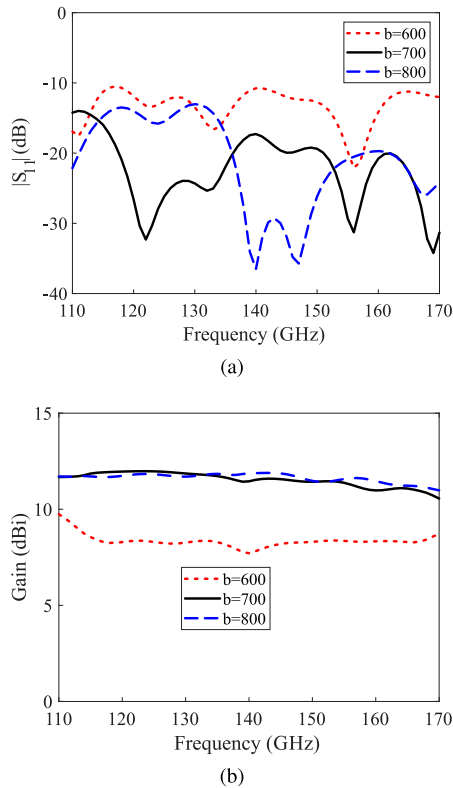

(a)

(b)

FIGURE 4. Simulated effect of variations in b on: (a) reflection coefficients, and (b) gain.

TABLE 1. Geometric parameters of the proposed design.

Parameter	Value (mm)	Parameter	Value
d	0.3	w	$1.15\ mm$
w_1	1.75	w_2	$0.5\ mm$
p_1	0.52	p_2	$0.5\ mm$
l_1	0.5	a	0.1
l_2	6	b	700
l_3	1.5		

form a SIW structure. The width of the SIW w is selected to propagate the TE_{10}-mode in the desired band. To form an elliptically tapered open-ended slot, an elliptical tapered metallic patch was separately connected to the top and bottom metals of the SIW line. The final geometry of the one sided tapered section was designed by first constructing a rectangle of dimensions $l_2 \times w_1$ and then subtracting an exponential surface from it. Fig. 1 depicts the equation for implementing the exponential surface. To create corrugations, nine rectangular slots with periodicity p_2 were carved on the outer sides
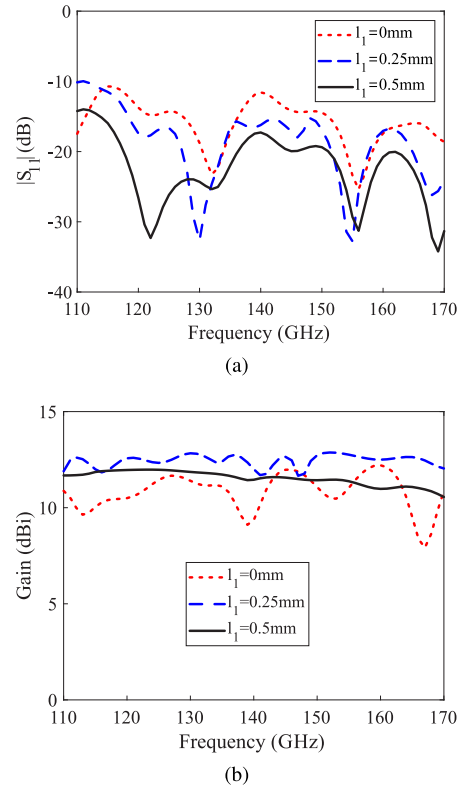

(a)

(b)

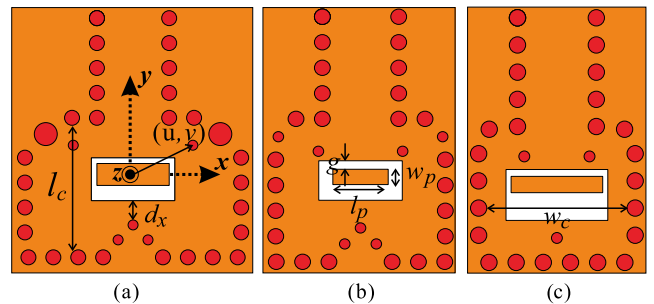**FIGURE 5.** Simulated effect of variations in l_1 on: (a) reflection coefficients, and (b) gain.

FIGURE 6. Geometries of the WG-PCB transitions. (a) Trans-I, (b) Trans-II, and (c) Trans-III.

TABLE 2. Geometric parameters of designed transitions in millimeters (mm).

Design	l_c	w_c	l_p	w_p	d_x	g	u	v
Trans-I	2.5	4.04	1.451	0.44	0.29	0.08	1.2	0.7
Trans-II	2.5	2.92	1.051	0.3	0.27	0.08	0.8	0.615
Trans-III	2.2	2.58	1.451	0.3	0.19	0.08	0.6	0.7

of each metallic patch. The length of the first eight slots is l_1, while the length of the ninth is reduced by 0.1 mm to meet fabrication tolerances.

Initially, a two-port simulation of the SIW line is performed to ensure that only TE_{10}-mode propagates within the frequency range of interest. Fig. 2 plots the propagation constant β versus frequency. The cut-off frequency (f_c) of the TE_{10} mode of the SIW line is 87.8 GHz. The f_c of the TE_{10}-mode
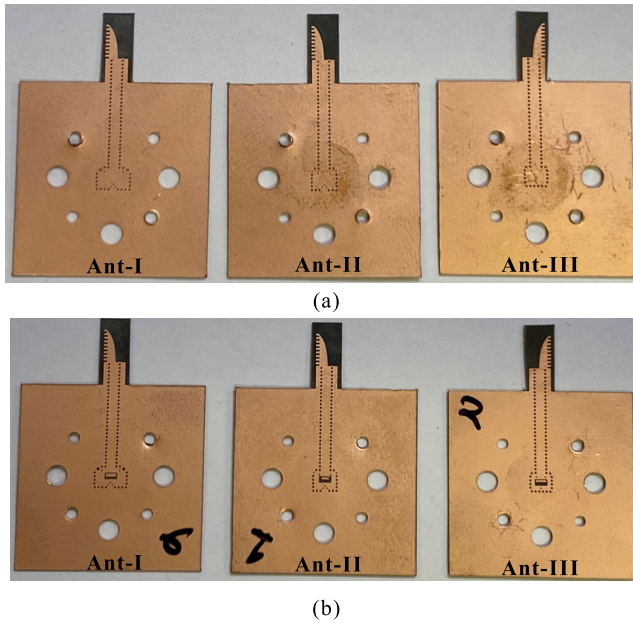
FIGURE 7. Fabricated prototypes of the Ant-I, Ant-II, and Ant-III: (a) Top view, and (b) bottom view.

can also be estimated from the width a of the SIW line using the following relation:

$$f_c = \frac{c}{2w\sqrt{\varepsilon_r}}, \qquad (1)$$

where c is the speed of light, w represents the width of the SIW line, and ε_r is the relative dielectric constant of the substrate. By plugging the values into (1), the calculated value is found to be 87.9 GHz.

The simulated magnitude of the E-field of the proposed antenna is presented in Fig. 3, which shows the TE_{10}-mode distribution inside the SIW line at 140 GHz.

B. PARAMETRIC STUDY

The parametric study is performed in Ansys Electronics Desktop 2021 software, with only one parameter being varied for analysis. The simulated effect of variations in parameter b on the reflection coefficients and gain is demonstrated in Fig. 4. The length of the tapered section that acts as a balun is controlled by parameter b, and thus the simulated reflection coefficients are affected. In terms of gain, increasing the value of b widens the tapered slot, which increases the aperture size and consequently the gain of the antenna. The optimum result is found for $b = 700$.

Fig. 5 depicts the parametric study to examine the effect of varying the length of corrugations l_1 on the simulated reflection coefficients and gain. The length l_1 affects the level of reflection coefficients across the entire band of interest, as shown in Fig. 5(a). In the absence of corrugations ($l_1=0$ mm), the level of the reflection coefficient is close to -10 dB near 118 GHz and 140 GHz. The level improves around 140 GHz for $l_1=0.25$ mm but degrades at 110 GHz.

The best result is obtained for $l_1 = 0.5$ mm. The l_1 affects the gain as well and for $l_1=0.5$ mm, there are fewer gain variations versus frequency across the entire band. Based on the optimization, the final geometric values of the design parameters are listed in Table 1.

C. MEASUREMENTS AND DISCUSSION

To evaluate the performance of the antenna, the single-layered SIW cavity-based WG-PCB transitions were designed. Due to the narrow passband response, three transitions termed as Trans-I, Trans-II, and Trans-III were designed to cover the whole D-band and their geometries as shown in Fig. 6. The length and width of the coupling slot are chosen to match those of the standard WR6.5 WG. The l_c and w_c denote the length and width of the coupling cavity, respectively. The parasitic patch having a length l_p and a width w_p is placed at a distance of g from the $+y$-directed edge of the coupling slot. The position of the symmetric vias inside the cavity is denoted by u and v along the x and y axes, respectively. Each transition is integrated separately with the proposed SIW ETSA and optimized for the frequency ranges of 110-130 GHz, 130-155 GHz, and 155-170 GHz. The disadvantage of these transitions is the narrow-band passband. As Trans-III is designed for the highest frequency range, the losses will be higher as compared to Trans-II and Trans-I. The optimized geometric parameters are tabulated in Table 2.

Ant-I, Ant-II, and Ant-III are the fabricated versions of the integrated antennas, and photographs are shown in Fig. 7. The fabrication precision of the trace-width, via-via spacing, and trace-gap were 0.1 mm, 0.2 mm, and 0.08 mm, respectively. The reflection coefficients of the prototypes were measured using the D-band VNA extenders with Keysight N5244B PNA-X network analyzer. A SOLT calibration was performed beforehand using the WR6.5 waveguide calibration kit. Fig. 8 depicts the comparison of the simulated and measured reflection coefficients. According to Fig. 8(a), the integrated antenna has a measured -10 dB IBW of 20 GHz (110–130 GHz). Similarly, the measured results for Fig. 8(b) and (c) yield -10 dB IBW of 28.6 GHz (130–158.6 GHz) and 16 GHz (154–170 GHz), respectively. The discrepancies between the simulated and measured results can be attributed to the fabrication tolerances and fixture misalignments when connecting the transitions with the WR6.5 waveguide.

The far-field measurement setup was constructed using the N5183B signal generator, WR6.5 SGx module, WR6.5 SAx module, D-band horn antenna, D-band WGs, and N9030A signal analyzer. The maximum output power of the WR6.5SGx module (P_{in}) was measured using the PM5B power meter while operating on 5v. The antennas for the transmitter (Tx) and receiver (Rx) antennas were separated by 1000 mm. The reference setup was created first to find the gain of the horn antenna. To find the received power (P_r) at the horn-WG interface, the connecting cable loss and conversion loss of the WR6.5 SAx module were also
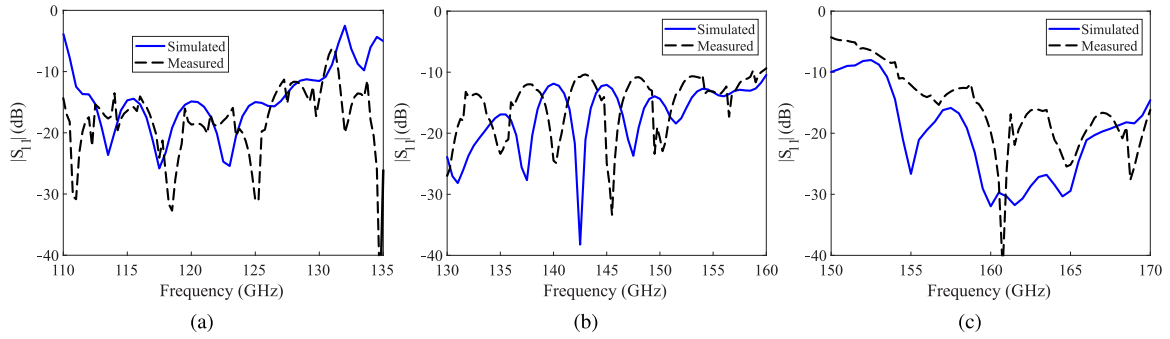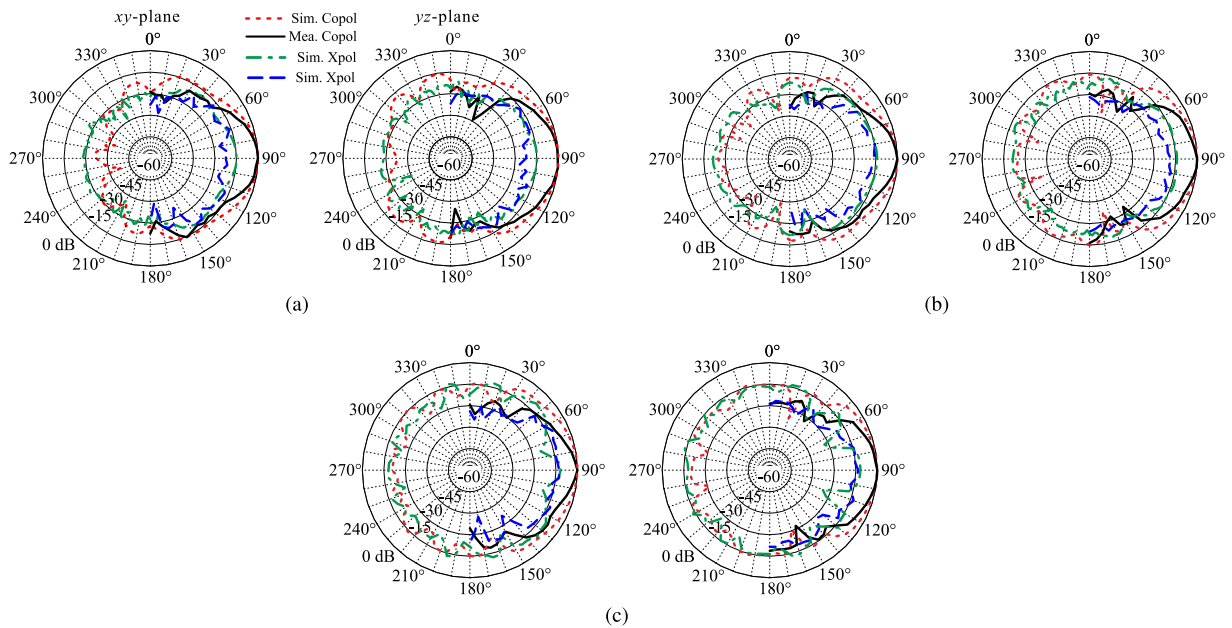
FIGURE 8. Comparison of the simulated and measured reflection coefficients of the proposed integrated antennas: (a) Ant-I, (b) Ant-II, and (c) Ant-III.
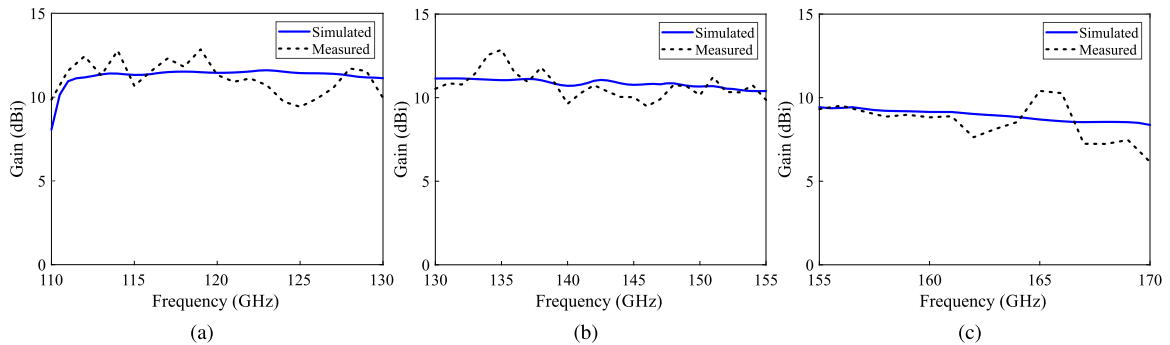
FIGURE 9. Comparison of the simulated and measured gains of the proposed integrated antennas: (a) Ant-I, (b) Ant-II, and (c) Ant-III.


FIGURE 10. Comparison of the simulated and measured radiation patterns: (a) 120 GHz. (b) 140 GHz, and (c) 160 GHz.

measured separately. The Friss equation was used to calculate the gain of the horn antenna. Afterward, the Rx horn was replaced by the individual antenna under test (AUT) to perform measurements for the gain in the end-fire direction

and radiation patterns in the *xy*- and *yz*-planes. It should be noted that the AUT was mounted on a rotating metallic stand that can be rotated only in the *xy*-plane in the range of ±90°. Additionally, in the *xy*-plane radiation pattern

TABLE 3. Comparison of the proposed D-band design with the earlier studies.

Ref. No.	Antenna Type	Fabrication method	−10 dB IBW (GHz) [%]	Peak Gain (dBi)	Cost	Radiation direction
[3]	Quasi-Yagi-Uda	130-nm SiGe BiCMOS with LBE	(135-165) [20]	5.1	High	End-fire
[4]	2×2 patch array	QFN for AiP	≈ (120–132) [9.5]	11.5	Medium	Broadside
[5]	1×2 folded dipole array	AiP	(118–136) [14.2]	9.7	Medium	Broadside
[6]	Slot with via-fence resonator	LTCC	(114-136) [17.6]	6 at 122.5 GHz	Medium	Broadside
[11]	SIW fed horn	3-D printing	(129.5–156.5) [18.9]	15.46	Medium	Broadside
	SIW fed patch	PCB	(125.3–154.4) [20.8]	7.26	Low	Broadside
[13]	1×8 Patch array	PCB	7GHz at 122 GHz	12.98	Low	Broadside
[16]	Slot in SIW	PCB	(110–170 [42.86]	10.8	Low	Broadside
Proposed	SIW ETSA	PCB	(110–130)[16.67]/ (130–155)[17.54]/ (155–170)[9.23]	12.85/12.86/10.4	Low	End-fire
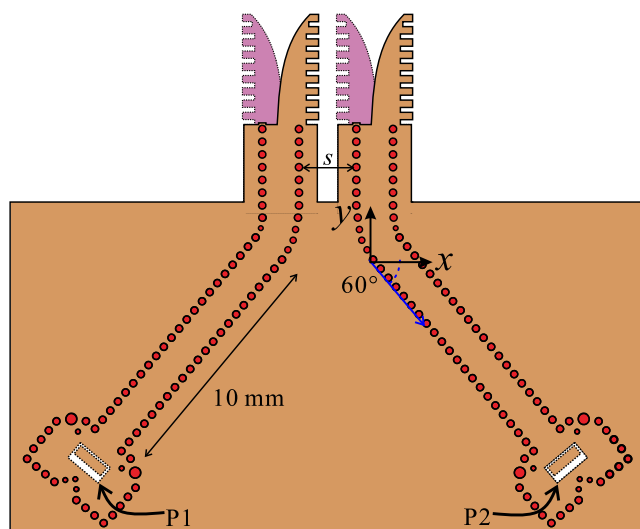
FIGURE 11. Geometry of the Ant-I based 2 × 2 MIMO antenna.
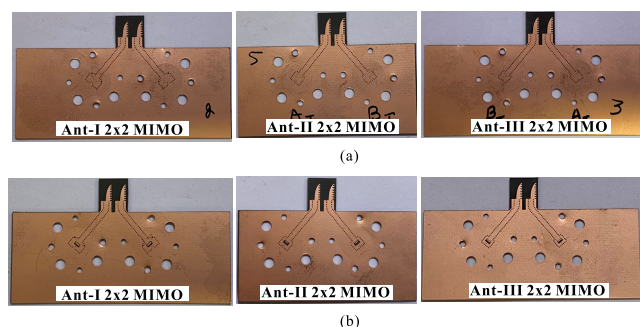
FIGURE 12. Fabricated prototypes of the 2 × 2 MIMO antennas: (a) Top view, and (b) bottom view.

measurements, E-plane WG bent was used to attach the AUT with the WR6.5 SGx module, and the Tx side E-plane orientation was changed from vertical to horizontal for the assessment of co-polarization (Copol) and cross-polarization (Xpol) radiation. For the yz-plane, an additional H-plane bent was used with the AUT while the orientation of the Tx horn was altered for accessing the Copol and Xpol radiation. The

comparisons of simulated and measured gains for all three integrated antennas are depicted in Fig. 9. It can be observed that the measured gain has a reasonable concurrence with the simulated results. The deviation is primarily due to the inaccuracies in the measurement setup arising from the manual work, misalignment between the Tx and Rx, and reflections from the rotating and fixed stands that were used on the Tx and Rx sides. Fig. 10 compares simulated and measured radiation patterns for the xy- and yz-planes at the frequencies of 120 GHz, 140 GHz, and 160 GHz. It can be observed that the measured Copol patterns are narrower than the simulated ones, which may be caused due to the presence of metallic stand and waveguide parts that were not considered in the simulations.

The comparison of the proposed work with the earlier D-band antennas is summarized in Table 3. A 130-nm SiGe BiCMOS process is used to design an on-chip Quasi-Yagi-Uda with LBE postprocessing [3]. The design is advantageous from the standpoint of chip integration because interconnect losses are reduced, but at the cost of expensive die area and additional complexity on account of LBE process. In [4], a 2 × 2 microstrip patch array is designed on an alumina substrate and fenced in a quad-flat-no-lead (QFN) package for AiP applications, resulting in a narrow −10 dB IBW and higher gain with a high fabrication cost. Similarly, an earlier work [5] designed a 2 × 2 folded dipole array on a polyimide substrate, with the package base designed in the LTCC process for the AiP solution. The design accomplished a −10 dB IBW of 14.2% and a peak gain of 9.7 dBi. In the LTCC process, a slot antenna with via fence was designed, yielding a −10 dB IBW of 17.6% and a gain of 6 dBi at 122.5 GHz. The authors presented two designs in [11], the first of which is a SIW cavity fed 3-D printed horn antenna with a −10 dB IBW and peak gain of 18.9% and 15.46 dBi, respectively. However, the design is not fit for low-profile applications due to its large size. The second study showed a SIW fed patch antenna fabricated using the standard PCB process that has a low-profile, −10 dB IBW of 20.8%, and a peak gain of 7.26 dBi. A differentially fed 1 × 8 microstrip patch array was designed for 122 GHz that achieved a narrow
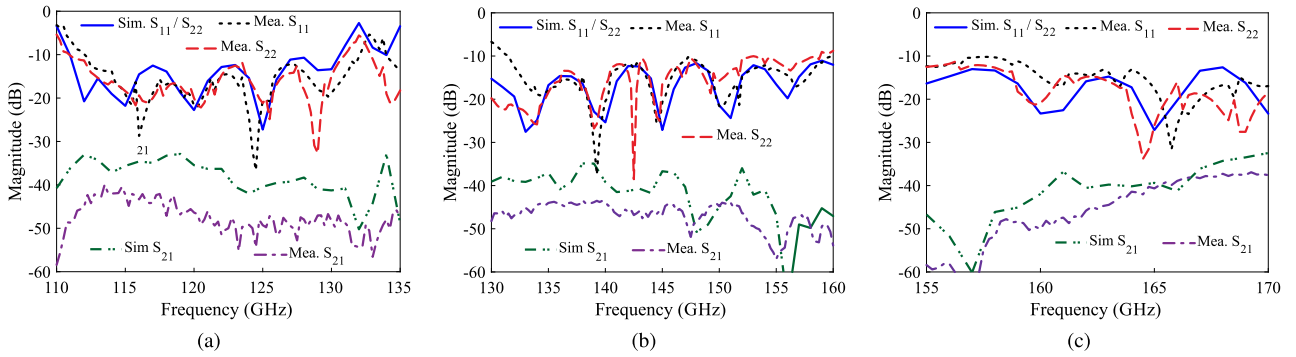
FIGURE 13. Comparison of the simulated and measured S-parameters of the 2 × 2 MIMO antennas based on: (a) Ant-I. (b) Ant-II, and (c) Ant-III.
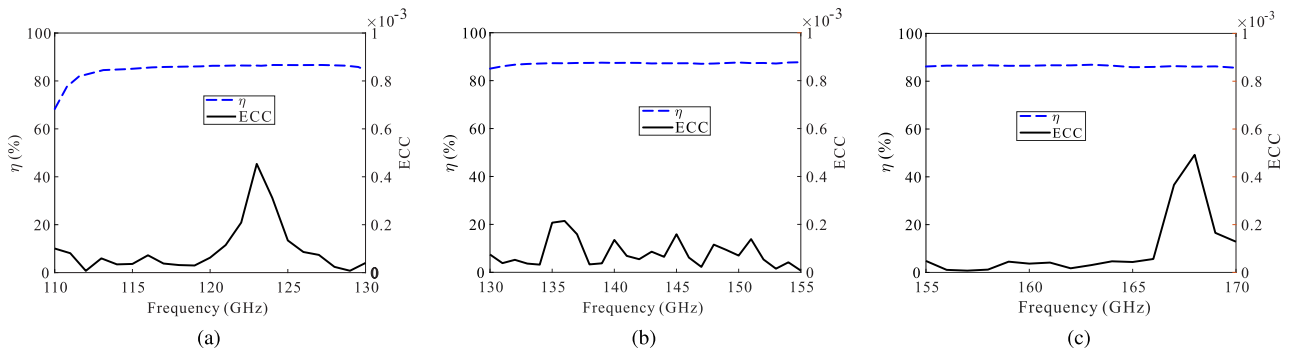

FIGURE 14. Simulated η and ECC of the 2 × 2 MIMO antennas based on: (a) Ant-I. (b) Ant-II, and (c) Ant-III.
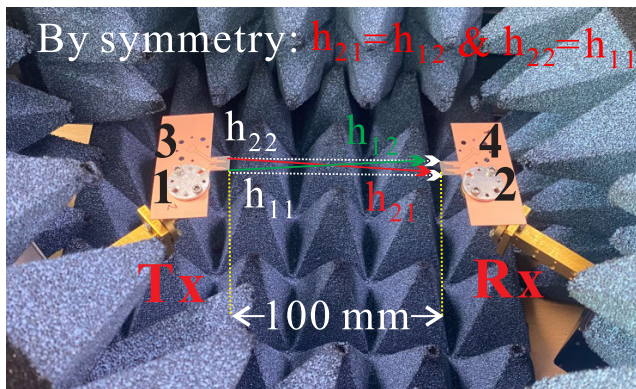

FIGURE 15. Measurement setup for condition number calculation.

−10 dB IBW of 7 GHz with a peak gain of 12.98 dBi. In [16], a PCB-based wideband slot antenna in SIW was designed where −10 dB IBW covers the whole D-band, and a peak gain of 10.8 dBi was achieved. The proposed antenna achieved a wider −10 dB IBW and a higher peak gain when compared to [3], [4], [5], and [6] and the second design of [11]. The 3-D printed horn antenna in an earlier study [11] and 1 × 8 patch array design of [13] achieved higher gains but lower −10 dB IBWs than the proposed work. In comparison to [16], the proposed design obtains the same −10 dB IBW but a higher peak gain. In terms of radiation

direction, the proposed and [3] are end-fire radiators, whereas the remaining designs are broadside radiators. Also note that the tabulated −10 dB IBWs for proposed design are written by avoiding overlapping values.

III. 2 × 2 MIMO ANTENNA DESIGN AND MEASUREMENTS

A. DESIGN DESCRIPTION

The 2 × 2 MIMO antenna was designed by integrating two antennas with the respective PCB-WG transitions. Fig. 11 shows the geometry of the Ant-I based 2 × 2 MIMO antenna. The edge-to-edge separation is denoted by $s = 2.25$ mm and each transition has a length of 10 mm concerning the axis. Considering the footprints of the WR6.5 WG, the transition is rotated by an angle of 60°. In the simulation and measurement, the energy is coupled to the antennas via ports P1 and P2.

B. MEASUREMENTS AND DISCUSSION

The 2 × 2 MIMO antennas were fabricated for performance evaluation and the photographs of the top and bottom views of the prototypes are depicted in Fig. 12. The reflection coefficients of all three 2 × 2 MIMO antennas were measured using the N5244B PNA-X network analyer with D-band extenders and the comparison of the simulation and measurement is shown in Fig. 13. The measured result of the reflection coefficients for all three designs agree reasonably well with the
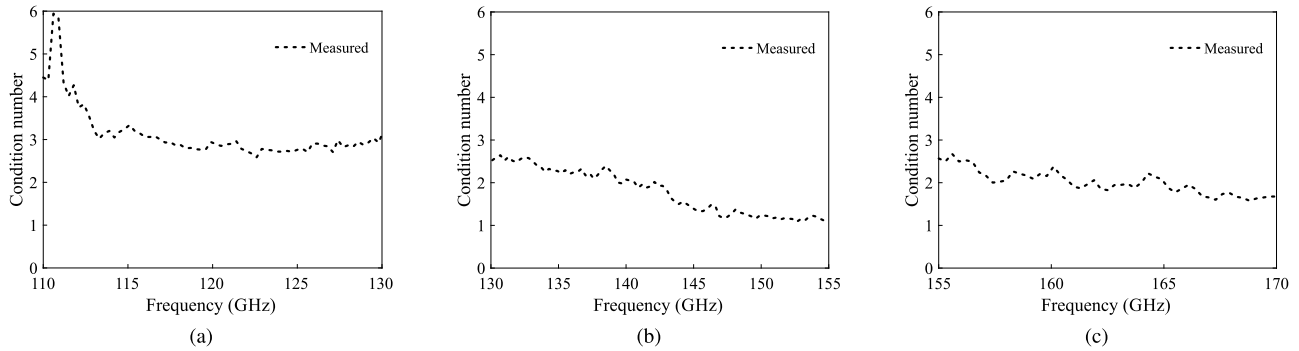
FIGURE 16. Measured condition number of the channel matrix for various 2 × 2 MIMO antennas: (a) Ant-I. (b) Ant-II, and (c) Ant-III.

simulation results, and the measured isolation between the ports is found to be > 36.9 dB. The discrepancies between the simulated and measured results can be attributed to the fabrication imperfections and the fixture issues.

Fig. 14 plots the simulated radiation efficiencies (η) and envelop correlation coefficient (ECC) of the proposed MIMO antennas. From the figures, $\eta > 80\%$ for all MIMO antennas within the measured -10 dB IBW. The simulated results of the ECC were obtained directly from the HFSS software using the built-in function. Generally, ECC values of < 0.5 are acceptable [17], [18], and in the proposed design, the values for all three antennas are lower than 0.0005

To calculate the condition number of a channel matrix H for the LOS MIMO application, we performed the S-parameter measurements of the fabricated prototypes. The condition number for channel matrix H is defined as follows [19]:

$$cond(H) = \frac{\lambda_{max}(H)}{\lambda_{min}(H)} \qquad (2)$$

where λ_{max} and λ_{min} represent the maximum and minimum singular values of the channel matrix H. A condition number closer to 1 is preferred to reduce the likelihood of error in the receiver. Fig. 15 shows the measurement setup that was constructed to evaluate the condition number. The antennas connected to the port1 and port2 of the N4244B PNA-X network analyzer are referred to as Tx and Rx antennas, respectively, that are separated by a distance of 100 mm. Tx antennas are numbered 1 and 3, while Rx antennas are numbered 2 and 4. From the setup shown in Fig. 15, each Rx antenna will receive a signal from 1 and 3. Due to the availability of a 2-port measurement system, the direct and cross path gain of the channel matrix (h_{11} and h_{12}) are measured by connecting port2 at 2 and 4, respectively. Furthermore, given the symmetry of the antennas, the values of 3 are $h_{12} = h_{21} =$ and $h_{22} = h_{11}$. Based on the measurement setup, the channel matrix for the 2 × 2 MIMO setup is shown below.

$$[H] = \begin{bmatrix} h_{11} & h_{12} \\ h_{21} & h_{22} \end{bmatrix} = \begin{bmatrix} |S_{21}|e^{j\theta_{21}} & |S_{41}|e^{j\theta_{41}} \\ |S_{41}|e^{j\theta_{41}} & |S_{21}|e^{j\theta_{21}} \end{bmatrix} \qquad (3)$$

where θ represents the angle in radians. Fig. 16 demonstrated the values of measured condition number that are obtained

using (3). For all graphs, the values of the condition number are found to be < 6.

IV. CONCLUSION
In this paper, single and 2 × 2 MIMO antennas were designed using SIW-based ETSA. The elliptical tapering profile and corrugation length were optimized to achieve low reflection coefficients in the D-band. For measurement purposes, three transitions that operate on different frequency ranges are designed and integrated with the proposed design. The measurement results of single integrated antennas cover the whole D-band for $|S_{11}| < -10$ dB with an overall gain > 6.15 dBi. The D-band 2 × 2 MIMO antennas were evaluated for the first time to the best of the authors' knowledge. The measurements were performed for the S-parameters of all three versions. Following that, two identical antennas separated by 100 mm were connected to the VNA extenders, and measurements were performed in a LOS MIMO environment to determine the complex coefficients of the channel matrix. The condition number for all three antennas is less than 6. The proposed design will be integrated with D-band MIMO transceiver for wireless demonstration.

REFERENCES
[1] A. Altaf and M. Seo, "A review of the D-band antennas," in *Proc. 14th Global Symp. Millimeter-Waves Terahertz (GSMM)*, May 2022, pp. 16–18.

[2] S. Pan and F. Capolino, "Design of a CMOS on-chip slot antenna with extremely flat cavity at 140 GHz," *IEEE Antennas Wireless Propag. Lett.*, vol. 10, pp. 827–830, 2011.

[3] W. T. Khan, A. C. Ulusoy, G. Dufour, M. Kaynak, B. Tillack, J. D. Cressler, and J. Papapolymerou, "A D-band micromachined end-fire antenna in 130-nm SiGe BiCMOS technology," *IEEE Trans. Antennas Propag.*, vol. 63, no. 6, pp. 2449–2459, Jun. 2015.

[4] S. Beer, H. Gulan, C. Rusch, and T. Zwick, "Coplanar 122-GHz antenna array with air cavity reflector for integration in plastic packages," *IEEE Antennas Wireless Propag. Lett.*, vol. 11, pp. 160–163, 2012.

[5] S. Beer, H. Gulan, C. Rusch, and T. Zwick, "Integrated 122-GHz antenna on a flexible polyimide substrate with flip chip interconnect," *IEEE Trans. Antennas Propag.*, vol. 61, no. 4, pp. 1564–1572, Apr. 2013.

[6] S. Beer, L. Pires, C. Rusch, J. Paaso, and T. Zwick, "A 122 GHz microstrip slot antenna with via-fence resonator in LTCC technology," in *Proc. 6th Eur. Conf. Antennas Propag. (EUCAP)*, Mar. 2012, pp. 1329–1332.

[7] S. B. Yeap, X. Qing, M. Sun, and Z. N. Chen, "140-GHz 2 × 2 SIW horn array on LTCC," in *Proc. IEEE Asia–Pacific Conf. Antennas Propag.*, Aug. 2012, pp. 279–280.

[8] Z. Qi, X. Li, J. Chu, J. Xiao, and H. Zhu, "High-gain cavity backed patch antenna arrays at 140 GHz based on LTCC technology," *Int. J. Microw. Wireless Technol.*, vol. 11, no. 8, pp. 829–834, Oct. 2019.

[9] D. Zarifi, A. Farahbakhsh, and A. U. Zaman, "A D-band center-feed linear slot array antenna based on gap waveguide," in *Proc. 13th Eur. Conf. Antennas Propag. (EuCAP)*, Mar. 2019, pp. 1–3.

[10] D. Kim, J. Hirokawa, M. Ando, J. Takeuchi, and A. Hirata, "64 × 64-element and 32 × 32-element slot array antennas using double-layer hollow-waveguide corporate-feed in the 120 Ghz band," *IEEE Trans. Antennas Propag.*, vol. 62, no. 3, pp. 1507–1512, Mar. 2014.

[11] C. Ma, S. Ma, L. Dai, Q. Zhang, H. Wang, and H. Yu, "Wideband and high-gain D-band antennas for next-generation short-distance wireless communication chips," *IEEE Trans. Antennas Propag.*, vol. 69, no. 7, pp. 3700–3708, Jul. 2021.

[12] C. Gu, S. Gao, V. Fusco, G. Gibbons, B. Sanz-Izquierdo, A. Standaert, P. Reynaert, W. Bösch, M. Gadringer, R. Xu, and X. Yang, "A D-band 3D-printed antenna," *IEEE Trans. Terahertz Sci. Technol.*, vol. 10, no. 5, pp. 433–442, Sep. 2020.

[13] R. Hasan, W. A. Ahmed, J. Lu, H. J. Ng, and D. Kissinger, "F-band differential microstrip patch antenna array and waveguide to differential microstrip line transition for FMCW radar sensor," *IEEE Sensors J.*, vol. 19, no. 15, pp. 6486–6496, Aug. 2019.

[14] H. H. Bae, T. H. Jang, H. Y. Kim, and C. S. Park, "Broadband 120 GHz L-probe differential feed dual-polarized patch antenna with soft surface," *IEEE Trans. Antennas Propag.*, vol. 69, no. 10, pp. 6185–6195, Oct. 2021.

[15] M. H. Maktoomi, Z. Wang, H. Wang, S. Saadat, P. Heydari, and H. Aghasi, "A sub-terahertz wideband stacked-patch antenna on a flexible printed circuit for 6G applications," *IEEE Trans. Antennas Propag.*, vol. 70, no. 11, pp. 10047–10061, Nov. 2022.

[16] A. Altaf, W. Abbas, and M. Seo, "A wideband SIW-based slot antenna for D-band applications," *IEEE Antennas Wireless Propag. Lett.*, vol. 20, no. 10, pp. 1868–1872, Oct. 2021.

[17] M. Li, Y. Zhang, F. Jiang, D. Wu, K. L. Yeung, L. Jiang, and R. Murch, "Improvement for MIMO systems by increasing antenna isolation and shaping radiation pattern using hybrid network," *IEEE Trans. Ind. Electron.*, vol. 69, no. 12, pp. 13891–13901, Dec. 2022.

[18] M. Li, Y. Zhang, D. Wu, K. L. Yeung, L. Jiang, and R. Murch, "Decoupling and matching network for dual-band MIMO antennas," *IEEE Trans. Antennas Propag.*, vol. 70, no. 3, pp. 1764–1775, Mar. 2022.

[19] L. Liu, W. Hong, H. Wang, G. Yang, N. Zhang, H. Zhao, J. Chang, C. Yu, X. Yu, H. Tang, H. Zhu, and L. Tian, "Characterization of line-of-sight MIMO channel for fixed wireless communications," *IEEE Antennas Wireless Propag. Lett.*, vol. 6, pp. 36–39, 2007.

AMIR ALTAF (Member, IEEE) received the B.S. degree in electrical engineering from the University of Engineering and Technology, Peshawar, Pakistan, in 2011, and the Ph.D. degree from the Division of Electronics and Electrical Engineering, Dongguk University, Seoul, South Korea, in 2018. Currently, he is a Senior RF Engineer with Millibeam, Eveleigh, Australia. From 2018 to 2023, he was with the Department of Electrical and Computer Engineering, Sungkyunkwan University, as a Post-Doctoral Researcher, and then a Research Professor. His research interests include circularly polarized antennas, reconfigurable dielectric resonator antennas, millimeter-wave on-chip antennas and filters circuits, D-band antennas, and 140 GHz power amplifiers. He is a member of the IEEE Antennas and Propagation Society.

MUNKYO SEO (Senior Member, IEEE) received the B.S. and M.S. degrees in electronics engineering from Seoul National University, Seoul, South Korea, in 1994 and 1996, respectively, and the Ph.D. degree in electrical engineering from the University of California at Santa Barbara (UCSB), Santa Barbara, CA, USA, in 2007. From 1997 to 2002, he was a RF Engineer with LG Electronics Inc., Anyang, South Korea, designing microwave subsystems for wireless communication. From 2009 to 2013, he was with Teledyne Scientific Company, Thousand Oaks, CA, USA, where he worked on the design of various millimeter-wave, terahertz, and high-speed mixed-signal circuits. In 2013, he joined the Department of Electrical and Computer Engineering, Sungkyunkwan University, Suwon, South Korea, where he is currently an Associate Professor.

• • •